

# Hydrogen-Induced Stress Cracking of Swaged Super Duplex Stainless Steel Subsea Components

M. Sofia Hazarabedian,\* Andreas Viereckl,\* Zakaria Quadir,\* Garry Leadbeater,\* Vladimir Golovanevskiy,\* Skjalg Erdal,\*\* Paul Georgeson,\*\* and Mariano Iannuzzi\*†

A recent subsea failure of two subsea connectors made of UNS S32760, a 25 wt% Cr super duplex stainless steel, led to an extensive root cause failure analysis. The components showed a single longitudinal crack along a swaged section, which arrested toward its thicker end. The brittle nature of the fracture surface, calcareous deposits on the component, and exposure to cathodic protection suggested hydrogen-induced stress cracking—a form of environmentally assisted cracking—as a plausible failure mechanism. Thus, the three causative factors promoting hydrogen-induced stress cracking, namely, a susceptible microstructure, a hydrogen bearing environment, as well as sufficiently high applied and residual stresses in the material were the focus of this investigation. This work details the material characterization work and presents a possible failure mechanism. The results showed that the failure developed from a combination of factors, typical for hydrogen-induced stress cracking. The measured hydrogen content in parts of the material exceeded 40 ppm, more than an order of magnitude higher than what is normally expected in super duplex stainless steels. Additionally, a highly anisotropic, coarse microstructure was observed, which in combination with the introduced cold-work from the swaging process and potential stress raisers from design and machining could have facilitated crack initiation, ultimately leading to the failure of the component. This hypothesis was reinforced by the presence of secondary cracks along the main, brittle fracture surface. Furthermore, mechanical testing results showed a detrimental effect on the material's properties due to the presence of residual hydrogen and the swaging operation.

KEY WORDS: hydrogen embrittlement, hydrogen induced stress cracking, oil and gas, subsea, super duplex stainless steel

## INTRODUCTION

Introduced in the late 1950s, duplex and super duplex stainless steels (DSS and SDSS, respectively) are widely used in many industries—including oil and gas—given their combination of mechanical, technological, and corrosion properties.<sup>1-3</sup> The microstructure of (S)DSS is composed of body-centered cubic ( $\alpha$ , bcc) ferrite and face-centered cubic ( $\gamma$ , fcc) austenite phases—both of which are stainless<sup>4</sup>—with an ideal 50%-50% ferrite-to-austenite balance.<sup>5</sup> (S)DSS have been found susceptible to hydrogen stress cracking (HSC) caused by cathodic protection (CP) or exposure to H<sub>2</sub>S-containing environments.<sup>6</sup>

### 1.1 | Hydrogen-Induced Stress Cracking of Duplex and Super Duplex Stainless Steels

HSC is a form of environmentally assisted cracking in which a ductile—albeit susceptible—material could exhibit fast brittle failure when exposed to hydrogen-bearing environments under particular loading conditions.<sup>7</sup> The term hydrogen induced stress cracking (HISC) is commonly used to refer to HSC of (S)DSS when exposed to hydrogen generated by CP.<sup>8</sup> HISC can occur at any potential below the reversible potential,  $E_{Rev}$ , of the hydrogen evolution reaction, which at pH 8.2 is

$E_{Rev} = -0.730 V_{SCE}$ .<sup>9</sup> Increased cathodic (i.e., more negative) potentials exacerbate HISC.<sup>10</sup>

(S)DSS have been shown to be particularly susceptible to HISC under specific settings. The first documented HISC incident was the BP-Amoco's Foinaven subsea hub connector failure,<sup>11</sup> followed shortly after by tie-in spool fractures in Amerada Hess and ConocoPhillips's Scott and Britannia fields.<sup>12</sup> Shell, Chevron, and Texaco experienced DSS and SDSS incidents between 2003 and 2004, all associated with forged components.<sup>6,13</sup> These failures led to a combined effort to minimize HISC and resulted in the interim NORSOK Workshop Agreement M-WA-01 published in 2005,<sup>14</sup> followed in 2008 by the first draft edition of DNV's DNVGL-RP-F112 Recommended Practice, which was revised in June 2018.<sup>15</sup> Additionally, in 2013, Statoil (Equinor) published lessons learned from several HISC cases involving forged tees, extruded pipes, and cold-formed, i.e., swaged, umbilical hose connectors.<sup>16</sup>

Today, there is consensus in that (i) the dual-phase structure with significant directionality of the phases, (ii) the austenite spacing, (iii) the presence of tertiary phases and intermetallic compounds (IMCs), (iv) the amount of cold work, and (v) the manufacturing route play decisive roles in the HISC resistance of (S)DSS. Regarding the role of the duplex  $\alpha/\gamma$  microstructure of (S)DSS, it is now well established that hydrogen diffuses predominantly through ferrite because hydrogen

Submitted for publication: February 10, 2019. Revised and accepted: April 3, 2019. Preprint available online: April 3, 2019, <https://doi.org/10.5006/3192>.

† Corresponding author. E-mail: [mariano.iannuzzi@curtin.edu.au](mailto:mariano.iannuzzi@curtin.edu.au).

\* Curtin University, Perth, Western Australia, 6102 Australia.

\*\* A60N, Perth, Western Australia, 6000 Australia.

solubility in the ferrite phase is lower than in austenite and given that the diffusivity is higher in the bcc than in the fcc crystal structure.<sup>17-18</sup> As a result, the distribution, morphology, and size of each phase affects the hydrogen diffusion path and, thereby, the overall HISC resistance.<sup>19-20</sup> In general, it is accepted that an  $\alpha$ -content above 50% could be detrimental to the overall HISC resistance.<sup>10</sup> Additionally, materials with a coarse-grain structure have been found to be more susceptible to HISC than those with a fine and equiaxed distribution of phases.<sup>8</sup> The improved HISC resistance of fine-grain duplex stainless steels has been attributed to a larger tortuosity for crack propagation.<sup>20-21</sup>

DNVGL-RP-F112 defines a coarse or fine microstructure based on the austenite spacing, i.e., the free ferrite path.<sup>22</sup> In this regard, the standard establishes that fine microstructures have an austenite spacing of 30  $\mu\text{m}$  or less. According to DNVGL-RP-F112, only DSS and SDSS components produced by hot isostatic pressing (HIP), tube and pipe of all sizes made by extrusion, seamless rolling or drawing, and rolled plates with less than 25-mm wall thickness can be initially assumed to be fine-grained, whereas forging and casting might result in coarse austenite spacing. The first edition of the DNVGL-RP-F112 Recommended Practice suggested measuring the austenite spacing in the likely crack propagation direction (in general, through-thickness), whereas the latest 2018 release removed any indication on the preferred sample orientation.<sup>22</sup> The current version of the Recommended Practice notes, nonetheless, that “when the ferrite grains are oriented perpendicular to the principal stresses, can give increased susceptibility to HISC. For items with an anisotropic grain structure (forged or rolled material) the manufacturing route should be reviewed to ensure a favorable grain flow.”<sup>22</sup>

Blanchard and collaborators have, however, shown that DSS with a similar austenite spacing can exhibit different HISC behaviors, depending on the microstructure and ferrite phase interconnectivity, which can accelerate hydrogen transport to the crack tip.<sup>23</sup> Therefore, the authors concluded, austenite spacing is not the only parameter that should be used to determine HISC susceptibility, suggesting that a method to quantify ferrite size, distribution, and connectivity is required.

The presence of tertiary phases and IMCs in the microstructure can further affect HISC resistance. In this regard, some of the reported failures have been in part attributed to the presence of chromium nitrides ( $\text{Cr}_2\text{N}$ ) at grain boundaries.<sup>16</sup> Similarly, severe cold-deformation by swaging was identified as one of the causative factors in Statoil (Equinor)’s SDSS hose coupling failure, leading the authors to conclude that duplex stainless steels might be unsuitable for swaging processes.<sup>16</sup>

Cold-work, either intentionally applied or as result of accidental damage, has been shown to negatively affect HISC resistance of the most common engineering alloys—including (S)DSS—used in O&G production, as illustrated by Treseder and Badrak.<sup>24</sup> Specifically for DSS, Chen, et al., found that in the presence of H, the elongation to failure dropped from 8.35% to around 2% when comparing solution annealed to cold-worked specimens. Hydrogen promoted transgranular cracking through ferrite and stepwise cracking for the austenite, with micro-cracks crossing the ferrite/austenite boundary. Moreover, Chen, et al.,<sup>25</sup> determined that cold worked specimens had a lower effective diffusivity and were more susceptible to hydrogen degradation. The authors suggested that cold-working led to

more hydrogen trapping sites due to a higher dislocation density. Similarly, in a  $\text{CO}_2 + \text{H}_2\text{S}$  environment, Crolet and Bonis showed a decrease in the critical chloride content for cracking with increased cold-working.<sup>26</sup> In contrast, Francis and collaborators showed that cold-working up to 35 HRC did not affect HISC performance of UNS S32760 as determined by slow strain rate testing.<sup>10</sup>

Lastly, given that fabrication directly influences the grain morphology, the  $\alpha/\gamma$  phase balance, the austenite spacing, as well as the presence of tertiary phases, significant differences in HISC performances have been reported between various manufacturing routes.<sup>6</sup> Lauvstad, et al., demonstrated that HIP (S)DSS led to the best HISC performance in seawater under CP.<sup>20</sup> There seems to be an agreement in that the HISC susceptibility increases in the following order: forging > rolled plates > HIP.<sup>6</sup> In this regard, HIP produces a homogeneous microstructure of equiaxed, fine austenite and ferrite grains while forging and rolling result in an anisotropic microstructure of elongated austenite islands in a ferrite matrix (i.e., a ribbon-like structure).<sup>23</sup>

## 1.2 | Component Failure Overview

This work focuses on two connectors used in subsea production equipment, both showing a single longitudinal crack in a swaged section. The components were manufactured from UNS S32760<sup>(1)</sup>, a 25 wt% Cr SDSS with a specified minimum yield strength (SMYS) of 550 MPa (80 ksi). The external surface of the connectors was exposed to a restricted flow of seawater and the components were in both electrical and electrolytic contact with a larger carbon steel subsea structure. The parts were subjected to CP, and substantial accumulations of calcareous deposits were found upon initial inspection.

The cracking extended along the swaged part of the component and the visual appearance suggested cleavage fracture and, hence, the possibility of a HISC failure. A comprehensive materials characterization that included positive material identification, fractography, microstructure analysis, microhardness mapping, total hydrogen concentration, as well as pitting corrosion and tensile testing was undertaken to address the three contributing factors of an environmentally assisted failure, namely, (i) the material and manufacturing routes, (ii) the presence of hydrogen, and (iii) the possibility of stress raiser and design considerations. The main findings of the analysis are presented herein.

## EXPERIMENTAL PROCEDURE

### 2.1 | Materials

The components, made from a forged and machined UNS S32760 bar, consisted of a stem with a cold swaged part attached (Figure 1). The swaged section had a cylindrical geometry with a variation in wall thickness from 2 mm to 11 mm and machined castellations on the internal surface. The swaged portion was first cut in half by abrasive waterjet cutting. Subsequently, specimens were extracted using electrical

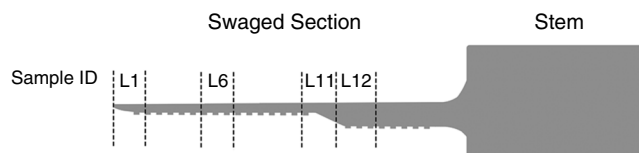


FIGURE 1. Schematic cross-section of the components and the main sample locations.

<sup>(1)</sup>UNS numbers are listed in *Metals and Alloys in the Unified Numbering System*, published by the Society of Automotive Engineers (SAE International) and cosponsored by ASTM International.

**Table 1. Electroetching Methods**

Method	Step	Solution Composition	Voltage (V) <sup>(A)</sup>	Time (s) <sup>(A)</sup>	Microstructural Constituents Revealed
A	1	20 g NaOH 100 mL H <sub>2</sub> O	1.5–2	12–30	Austenite-ferrite contrast intermetallic phases
B	1	10 g Oxalic acid 100 mL H <sub>2</sub> O	5–5.5	3–5	Chromium nitride precipitation
	2	20 g NaOH 100 mL H <sub>2</sub> O	1.5–2	10–30	Austenite-ferrite contrast intermetallic phases

<sup>(A)</sup> The voltage and time used depended on the exposed area of the metallographic specimens that in this study were between 22 mm<sup>2</sup> and 200 mm<sup>2</sup> approximately

discharge machining (EDM) and conventional cutting and machining operations. Figure 1 illustrates the locations of the main test samples used in this work. The direction and orientation terminology used herein adheres to the recommendations of ASTM E112.<sup>27</sup>

## 2.2 | Chemical Analysis

The composition of the material was verified by energy dispersive x-ray spectroscopy (EDS). A specimen was polished in the transverse-longitudinal (T-L) plane down to a 1 μm finish with diamond suspension, sonicated in ethyl alcohol, and stored overnight in a desiccator. The alloy composition was established as an average of the seven randomly collected EDS spectra at 20 kV and a working distance of 15 mm.

## 2.3 | Metallographic Preparation and Analysis

The microstructure characterization was performed using both light optical microscopy (LOM) and field emission-scanning electron microscopy (FE-SEM) coupled with EDS and electron backscatter diffraction (EBSD). The metallographic analysis included the assessment of austenite/ferrite volume fractions, austenite region size and anisotropy index, and austenite interspace in the through-thickness and longitudinal directions (L-S plane). The austenite region size and the anisotropy index were obtained by the Lineal Intercept Method,<sup>28</sup> whereas DNVGL-RP-F112 was followed for the austenite interspace.<sup>22</sup> Finally, the austenite-ferrite area fractions were quantified with EBSD. Area fractions are assumed proportional to the volume fraction.

For the metallographic analysis, samples were cut by EDM from both the swaged portion and the stem in the principal planes (L-S, S-T, and T-L) at different sections including the cross section of the main crack close to the suspected crack arrest location. Before mounting, carbon paint and copper tape were used to establish the samples' electrical connection for the subsequent electroetching. Specimens were mounted with a cold-curing epoxy resin and cured for at least 15 h. The crack cross-section specimens were cured under vacuum to avoid the formation of air bubbles inside the crack void. After mounting, the samples were mechanically ground and polished down to a 1 μm finish in diamond suspension using conventional metallographic wet surface preparation procedures. Samples were electroetched immediately after polishing as per the ASTM A923-14 standard and Statoil (Equinor)'s Technical note MAT-2010080.<sup>29-30</sup> Electroetching was done using a stainless steel cathode. Table 1 summarizes the different electroetching procedures, which were selected depending on the microstructural features to be studied.

## 2.4 | Fractography

The fracture surfaces were studied using FE-SEM secondary electron (SE) imaging at 5 kV, 15 kV, and 20 kV, in both Depth and Resolution modes with a working distance between

15 mm and 45 mm. EBSD was also used to study the cross section of the main crack close to its visible endpoint. The sample preparation process consisted in mechanical polishing up to 0.25 μm, followed by vibration polishing and ion milling to minimize and remove the stresses added during polishing. Before analysis, fracture surfaces were sonicated in ethanol, rinsed with deionized (18.2 MΩ) water, and subsequently dried with compressed air.

## 2.5 | Total Hydrogen Content

Melt extraction was used to measure the total hydrogen content of four samples, two from the thin and two from the thick part of the swaged portion of the component, with weights between 0.4022 g and 0.8216 g. The samples were cut from a comparable distance from the outer surface to minimize variations caused by hydrogen transport during exposure in service. The trapped hydrogen was released and taken up by the carrier gas (nitrogen) by isothermally treating the samples at 1,550°C in a graphite crucible in a pulse furnace. The thermal conductivity of the gas was measured and compared to a reference carrier gas. The hydrogen content of the sample is proportional to the difference between the two thermal conductivities and is calculated with the time integral of the signal.

## 2.6 | Microhardness Testing

To compare the mechanical properties along the specimen, Vickers microhardness (HV0.2) profiles were measured on the L-S plane of polished and etched samples along the swaged portion and on samples extracted from the stem as per ASTM E384-17.<sup>31</sup> The applied load was 200 gf (1.96 N), and care was taken to ensure the test surface was oriented perpendicular to the Vickers indenter for optimum accuracy. Additionally, the potential effect of the hydrogen content on the mechanical properties of each phase was evaluated by measuring the Vickers microhardness (HV0.1) of the austenite and ferrite along the L-S plane of the swaged section before and after a bake-out thermal treatment performed at 175°C for 48 h to remove diffusible H as detailed below. In this test, the applied load was 100 gf (0.98 N) to produce a smaller indent and reduce the probability of measuring the combined hardness of both phases.<sup>32</sup>

## 2.7 | Tensile Testing

Tensile tests were performed on custom samples machined from the swaged section as per ASTM E8/E8M.<sup>33</sup> Firstly, strips were cut along the swaged section in the S-T direction to simulate the hoop stress orientation the component experienced in service. After removing the castellations, the strips were flattened using a bench press. Eight rectangular subsized specimens were machined as close as possible from the outer surface of the flattened swaged section with a width of 7 mm and 2.5 mm thickness in the reduced gauge length section (Figure 2). The samples were inspected with dye penetrants after bending and machining to ensure the absence of cracks.

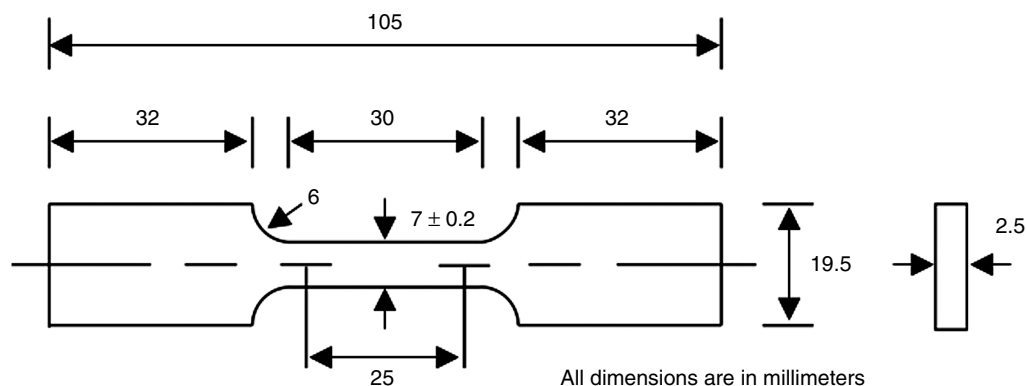


FIGURE 2. Custom tensile test specimen dimensions.

Table 2. Nominal UNS S32760 and Average Alloy Chemical Composition Measured by EDS

Condition	Elements (wt%)							
	Cr	Mn max.	Fe	Ni	Cu	Mo	W	N <sup>(A)</sup>
ASTM A790	24–26	1.00	Bal.	6.0–8.0	0.5–1.0	3.0–4.0	0.5–1.0	0.2–0.3
Measured	26.85	0.73	60.86	6.98	0.57	3.13	0.61	—

<sup>(A)</sup> Cannot be determined by EDS.

Finally, four of the machined samples (two from the thin and two from the thick section of the swaged section) were heat treated at 175°C for 48 h to remove trapped hydrogen from the material—an operation frequently referred to as hydrogen bake-out—to study the influence of hydrogen on the tensile properties. To separate the two possible effects of the bake-out treatment, i.e., the hydrogen removal and the relief of stresses that might occur during heating at 175°C, an additional control sample was baked-out before machining and flattening.

Strain gauges were attached to the gauge section for improved accuracy in the elastic region of the tensile tests. The constant test speed was 0.5 mm/min, which equates to a strain rate of approximately 0.015 mm/min as recommended in ASTM E8/E8M.<sup>33</sup> The measured load-displacement data was, then, converted to engineering stress-strain curves and the mechanical properties further analyzed.

### 2.8 | Corrosion Testing

Corrosion testing was performed according to Test Method C of the ASTM A923-14 standard.<sup>30</sup> Two approximately 25 mm × 25 mm × 5 mm specimens were cut with a diamond saw from the middle section of the swaged section. Additionally, all faces of the samples except from the inner surface were polished down to a 1 μm finish with diamond suspension to avoid localized corrosion due to the cutting method. Samples were immersed in the test solution prepared by dissolving 100 g of reagent-grade ferric chloride hexahydrate, FeCl<sub>3</sub>·6H<sub>2</sub>O, in 900 mL of 18.2 MΩ distilled water (approximately 6 % FeCl<sub>3</sub> by weight) at 50°C for 1 d.

## RESULTS

### 3.1 | Chemical Composition

Table 2 summarizes the average alloy chemical composition determined by EDS as well as the nominal standard composition of UNS S32760. The nitrogen content, in contrast,

cannot be reliably estimated by EDS and requires combustion, inert gas, or wet chemistry methods.<sup>34</sup>

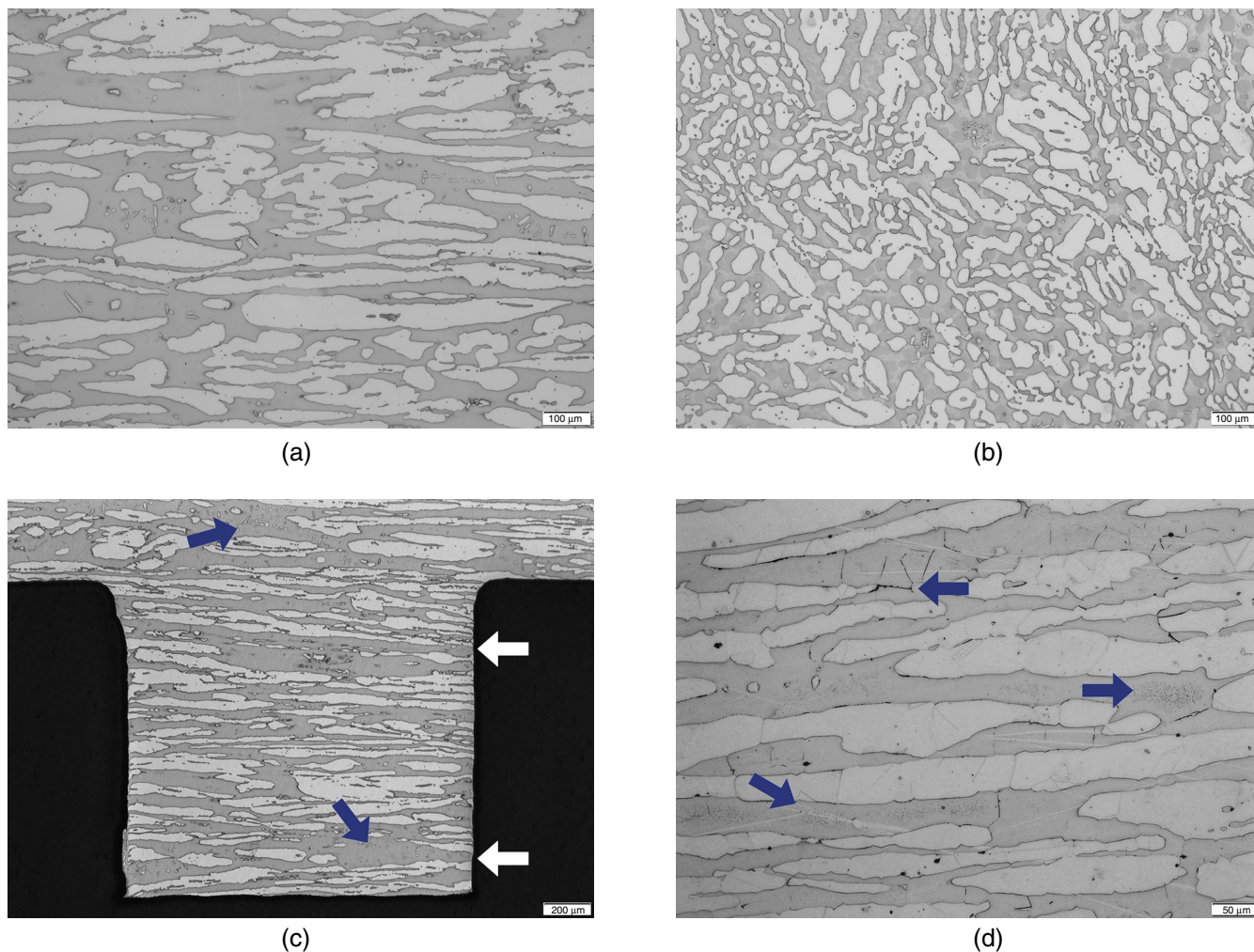
### 3.2 | Metallographic Characterization

Table 3 summarizes the austenite region size and anisotropy index as well as the austenitic interspacing. Electroetching revealed a highly anisotropic two-phase microstructure consistent with a SDSS microstructure, as indicated in Figures 3(a) and (b). Although the austenitic spacing through-thickness did not exceed the suggested value in the DNVGL-RP-F112 Recommended Practice, the values measured in the longitudinal direction were up to six times higher.<sup>22</sup> Clusters of small equiaxed austenite grains, present in large ferrite regions, were observed along the entire swaged section (Figure 3(c)). Furthermore, the structure revealed isolated indications of IMCs at grain boundaries and suspected intragranular chromium nitrides (Cr<sub>2</sub>N)

Table 3. Summary of the Metallographic Analysis

Parameter	Sample ID			
	L1	L11	L12	Stem
Sample thickness (mm)	2.1	5.2	10.4	—
Austenite region size	G 5.0	G 5.0	G 5.0	G 5.0
Austenite region mean intercept (μm)	60.3	56.9	54.8	53.7
Austenite region anisotropy index	6.12	5.75	5.16	5.70
Through-thickness austenitic spacing (μm) <sup>(A)</sup>	27.4	24.9	25.9	22.6
Longitudinal austenitic spacing (μm) <sup>(A)</sup>	184.8	143.5	134.2	127.9

<sup>(A)</sup> Measured in the L-S plane.



**FIGURE 3.** LOM of the dual phase SDSS swaged microstructure in the L-S plane for (a), (c), and (d) and S-T plane for (b). Samples in (a), (b), and (c) were etched with the Method A while the microstructure in (d) was revealed with the Method B (Table 1). Bright and dark phases correspond to austenitic and ferritic grains, respectively. In (c), the white arrows indicate ferrite islands that extended from end-to-end of the castellation while the blue arrows show the equiaxed austenite phase present in clusters. Likewise, the arrows point to the location of suspected carbides and intergranular precipitates in (d).

(Figure 3[d]). Therefore, the microstructure was classified as being possibly affected in accordance with Test Method A of the ASTM A923-14 standard.<sup>30</sup>

EBSD analysis (Figure 4) revealed the actual grain structures within each austenite and ferrite region. The austenite and ferrite volume fractions were 55.1 vol% and 44.9 vol%, respectively, as quantified by EBSD, within the acceptable values for (S)DSS.<sup>5</sup>

### 3.3 | Fractography

The main crack propagated longitudinally, arresting close to the thick end of the swaged section and extended further on the outer than on the inner surface. Additionally, plastic deformation and longitudinal secondary cracks were found along the inner surface of the swaged portion next to the main crack (Figure 5). Figure 6 summarizes the fracture surface characterization of the main crack. Figures 6(b) through (d) show cleavage, mixed cleavage/dimple rupture, and dimple rupture fracture surfaces, respectively. SEM analysis suggested that the fracture surface was predominantly

cleavage with mixed cleavage/rupture and dimpled rupture areas at the thin end of the swaged section and in some areas near the inner surface (Figure 6[b]). Pure cleavage fracture and secondary cracking were observed adjacent to the first castellation (Figures 6[e] and [f]).

Figures 7 through 9 present LOM, SEM, and EBSD results of the main crack in cross-section, respectively. In the EBSD maps in Figure 9, the black lines indicate zero resolution, i.e., the diffraction patterns from those points are poor in clarity due to deformation or there is no material present (e.g., voids and cracks). White boxes were superimposed on the EBSD maps to facilitate differentiating the crack from the deformed areas. Nevertheless, there was a small degree of mismatch due to sample drifting during the overnight EBSD data acquisition.

### 3.4 | Total Hydrogen Concentration Measurement

Table 4 details the results of the average total hydrogen measurements, showing a significantly higher mean hydrogen content in the thinner section of the swaged component

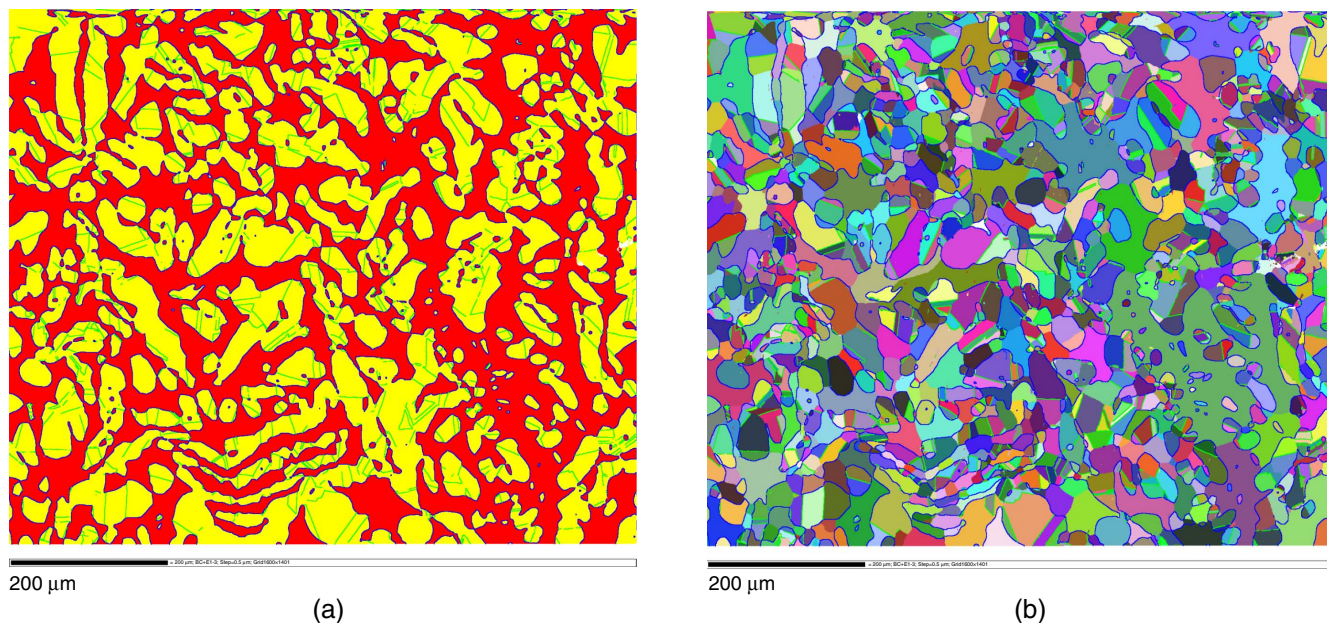


**FIGURE 4.** EBSD analysis of (fcc) austenite and (bcc) ferrite volume fraction. (a) Phase map. bcc: red, fcc: yellow. Blue lines: phase boundaries, black lines: grain boundaries (sample preparation artifacts removed). (b) Grains are plotted in random coloring. A comparison with (a) and (b) shows multiple grains within the same phase field.  $\langle 111 \rangle$   $60^\circ$  twin boundaries are superimposed in lime green.

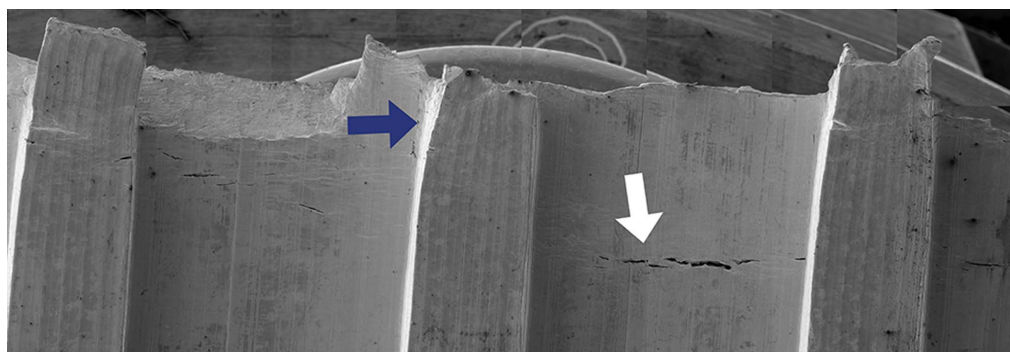


**FIGURE 5.** SE FE-SEM image showing secondary cracks (white arrow) and plastic deformation (dark arrow) on the internal surface.

compared with the thick section. In this regard, Lauvstad, et al., reported average total H contents of 11 ppm and 18 ppm measured using an identical method for HIP and forged SDSS, respectively.<sup>20</sup> Morana and collaborators have recently determined diffusible hydrogen content measurements of two pull-heads from retrieved subsea equipment after 12 y of service under CP at  $-1.1 V_{SCE}$ . Values ranged from 120 ppm to 20 ppm, decreasing towards the bulk of the samples. Almost no H was detected at the center of the 10 in. and 8 in. (bore size) components.<sup>35</sup>

### 3.5 | Microhardness Testing

The average Vickers microhardness (HV0.2) results are shown in Table 5 for the hardness profiles taken along the swaged section and a sample from the stem to compare the mechanical properties along the entire component. The microhardness value of the stem was  $268 \pm 17$  HV0.2. The highest microhardness values were observed in the transition area between the thick and the thin part of the swaged section with  $364 \pm 11$  HV0.2 and  $348 \pm 26$  HV0.2 for Profile 4 and Profile 5, respectively. These hardness values represent a 35% increase

in hardness from the hardest section of the swaged section compared to the forged but not swaged stem. Microhardness results towards the thinner section of the swaged section were  $313 \pm 13$  HV0.2,  $318 \pm 16$  HV0.2, and  $322 \pm 22$  HV0.2 for Profiles 1, 2, and 3, respectively.

Figure 10 illustrates the individual hardness profiles through-thickness of the swaged region for each location from the outside (i.e.,  $x = 0$  mm) to the inner surfaces. No clear trend in hardness was observed by comparing the inner and the outer surface of the component. However, as illustrated in Figure 10, the majority of the microhardness values for the transition portion (thin-to-thick) of the swaged section (Profiles 4 and 5) were above 350 HV, which is the maximum allowable hardness suggested in the DNVGL-RP-B401 standard for components exposed to CP.<sup>36</sup> The scattering of the data was attributed to the ferritic-austenitic microstructure of UNS S32760 and the dissimilar hardness of the ferrite and austenite phases.

Figure 11 shows the microhardness (HV0.1) results of austenite and ferrite regions before and after hydrogen removal, taken in an effort to study a possible dissimilar hardening

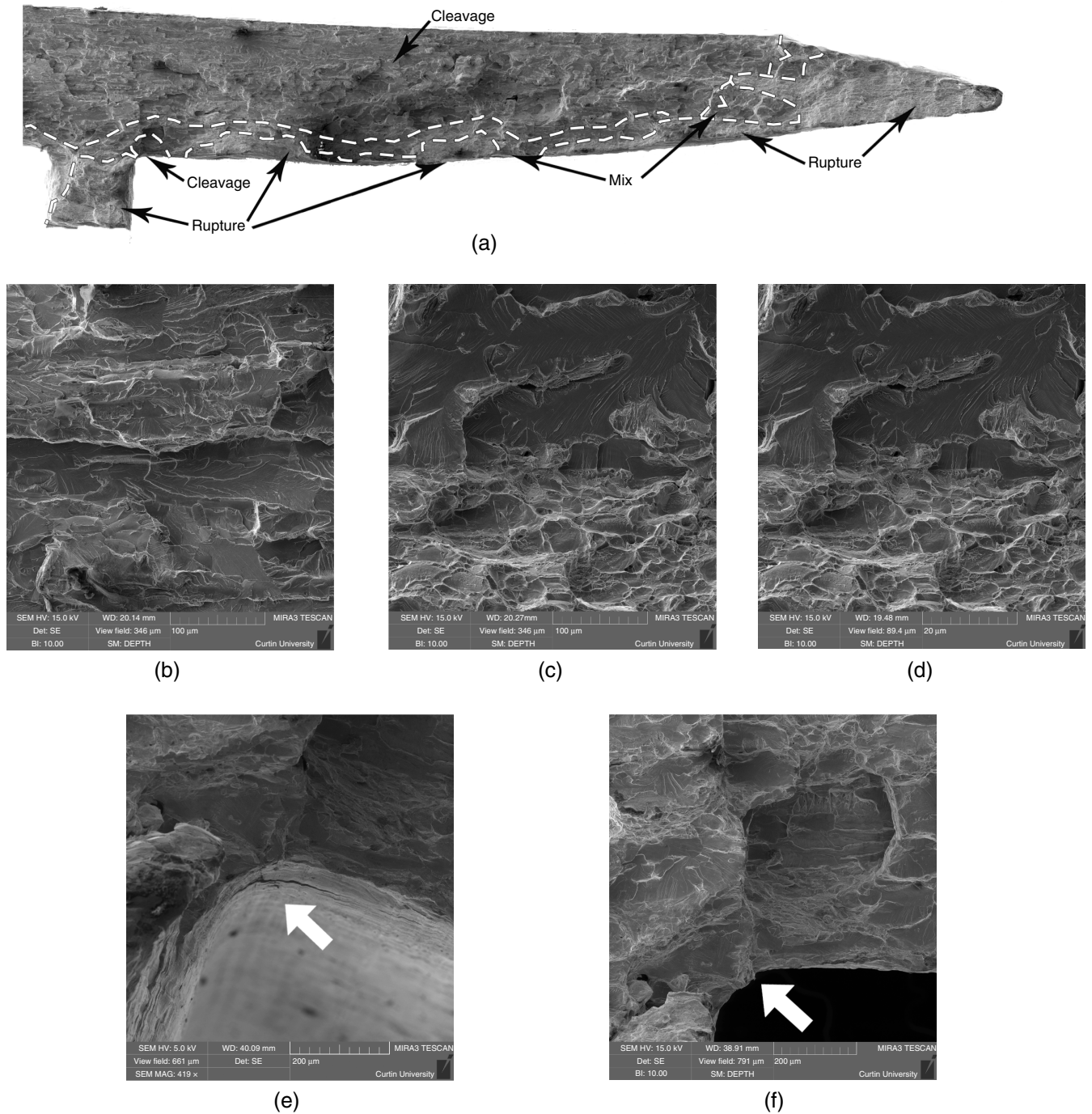


**FIGURE 6.** SEM SE images of the fracture surface at (a) the thin swaged end showing (b) cleavage, (c) cleavage/rupture mix, and (d) dimple rupture. (e) illustrates a secondary crack in the first castellation close to (g) the fracture surface. White arrows point to the secondary crack location.

effect of hydrogen on austenite and ferrite. As inferred from the statistical analysis presented in Figure 11, no clear trend was observed, suggesting no preferential effect of hydrogen on the hardness of both phases under the testing conditions. Kivisäkk,<sup>37</sup> in contrast, found a selective hardening of ferrite grains after hydrogen charging of fine-grained (i.e., extruded tube and small diameter bar) SDSS, whereas microhardness values of austenite were higher for a large diameter, coarse-grained forged bar SDSS. The authors speculated that the difference could be attributed to a low stress concentration in austenite on

fine-grained microstructures. However, these observations have not been corroborated in subsequent investigations.

### 3.6 | Tensile Testing

The tensile test results are summarized in Table 6 and representative stress-strain curves illustrated in Figure 12. The four tensile test samples in the nonbaked condition showed a brittle failure with elongation to fracture values of 1.15% to 1.66%. This is atypically low for SDSS and the S32760 alloy, which generally exhibit elongation to rupture values exceeding 25% for

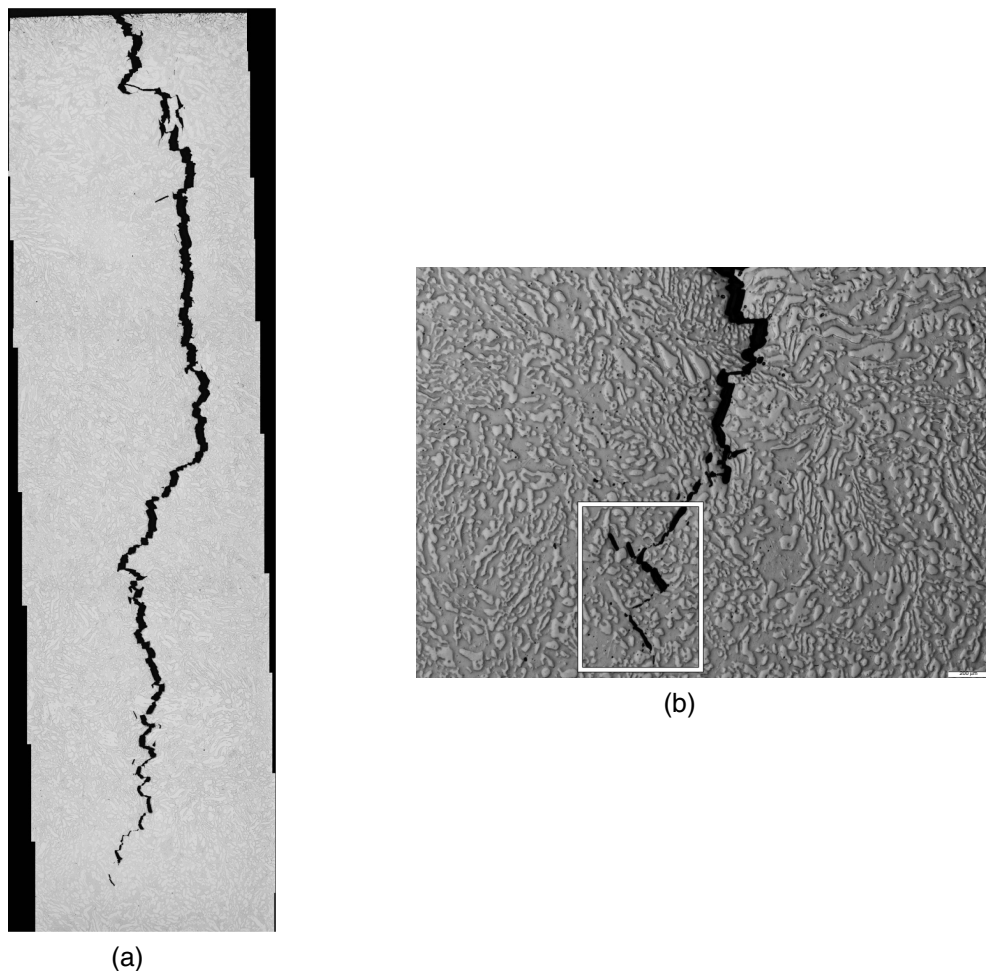


**FIGURE 7.** LOM of the cross section near the arrest location of the main crack: (a) full through-thickness crack propagation and (b) higher magnification detail of the apparent crack termination. The white box in (b) indicates the area of the SEM SE image and EBSD analysis in Figures 8 and 9.

forgings and pipes<sup>38-39</sup> and 16% for cold-worked fasteners.<sup>40</sup> Baked-out samples from the thin part of the swaged section showed an increase in plastic deformation with an elongation to fracture of 4.78% and 4.11% for samples T-E and T-F, respectively. Hydrogen bake-out resulted in an increase of elongation to fracture between 150% and 315% compared to the nonbaked samples. Ultimate tensile strength also increased for the baked specimens. Likewise, the control sample that was baked-out before flattening, showed an elongation to fracture of 5.31%, similar to that of the samples T-E and T-F. Assuming areas from where the specimens were extracted were subjected to the same degree of swaging, these findings suggested that the presence of hydrogen was responsible for the decrease in the tensile properties.

Both baked-out samples from the thick section (samples T-Y and T-Z) showed a predominantly ductile failure with an elongation to fracture of 10.27% and 21.35% for samples T-Y and T-Z, respectively. Sample T-Z exhibited an elongation to fracture value close to the specification in ASTM A1049/A1049M-18 for forged S32760 alloys, likely indicating a lower degree of cold-work.<sup>38</sup> The increase in elongation to fracture of the baked-out samples from the thick section compared to the thin section may indicate a detrimental effect of the swaging process on the mechanical properties of the material, which

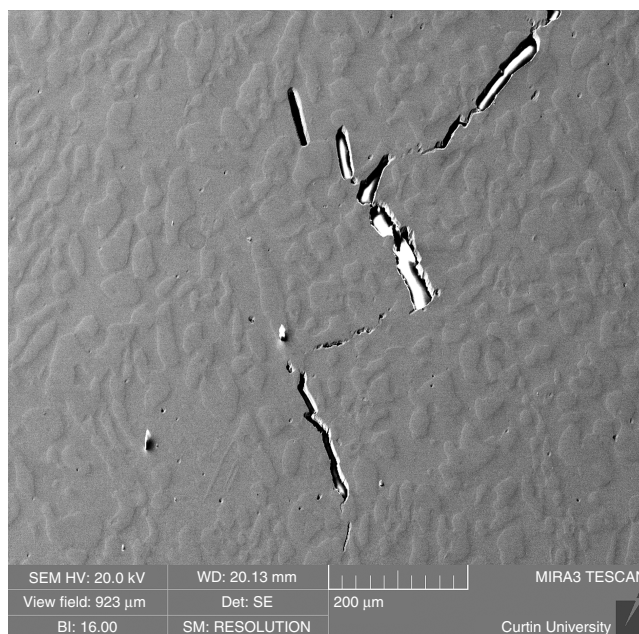


**FIGURE 8.** SEM SE image of the cross section near the arrest location of the main crack where the EBSD analysis of Figure 9 was performed.

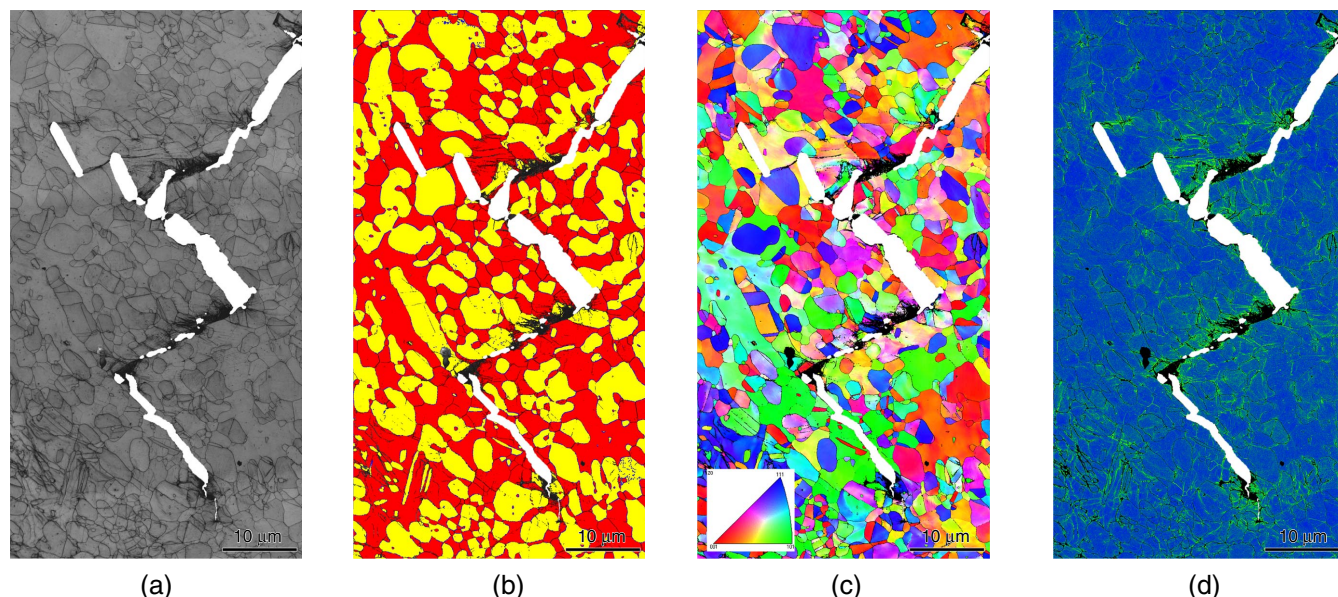


**FIGURE 9.** EBSD analysis of the cross section near the arrest location of the main crack indicated by the white box in Figure 7(b). The approximate area of the crack as seen in the Figure 8 is plotted in white. (a) BC map in grayscale and black represent the indexed and unindexed areas (i.e., lattice defects such as grain boundaries or deformation lines), respectively; (b) EBSD phase map where red: ferrite, yellow: austenite, and blue lines: phase boundaries; (c) Z direction IPF coloring orientation map; (d) KAM map indicating misorientation within the grains.

**Table 4. Hydrogen Content Results**

Sample ID	Swaged Section	Weight (g)	Hydrogen Content (ppm)
A-1	Thin portion	0.8216	44.57
A-1	Thin portion	0.4022	37.82
B-1	Thick portion	0.5270	4.23
B-2	Thick portion	0.4387	4.72

**Table 5. Vickers Microhardness Averages Measured along the Swaged Section and the Stem**

Parameter	Sample ID					
	L1		L6	L11	L12	Stem
	Profile 1	Profile 2	Profile 3	Profile 4	Profile 5	—
HV0.2	313±13	318±16	322±22	364±11	348±26	268±17

introduced an incremental amount of cold deformation from the thick to the thin end of the swaged portion of the component. The same trend was observed when evaluating the modulus of toughness of the nonbaked and baked-out tensile test samples. The modulus of toughness—determined as the integral of the stress-strain curve—is an important measure as it relates to the degree of deformation work a material can withstand until fracture in the case of overloading. The comparatively low values for the nonbaked samples versus the baked-out specimens also indicated the influence of residual hydrogen and swaging on the material's performance (Table 6).

Figures 13(a) and (b) show the fracture surface profile through-thickness of the tensile samples T-A and T-Z, respectively. For sample T-A, the fracture was predominantly cleavage and mixed close to the outer surface while the inner surface was identified as rupture (Figure 13[a]). The fracture

modes and their distribution presented several similarities with those observed at the main crack of the failed component (Figure 6). In contrast, the baked-out sample T-Z from the thick part of the swaged section had a rupture fracture morphology consistent with the ductile failure observed in the tensile tests (Figure 13[b]). Several random cleavage areas in predominantly rupture regions were found in sample T-E and, to a lesser extent, in samples T-A and T-Y. These cleavage areas were characterized by the presence of inclusions rich in Ca, Si, Al, O, and Mg, aligned in the L direction (Figures 13[c] and [d]).

### 3.7 | Corrosion Testing

As the component microstructure was identified as being “possibly affected” by the precipitation of intergranular phases according to the categorization given in Test Method A of the

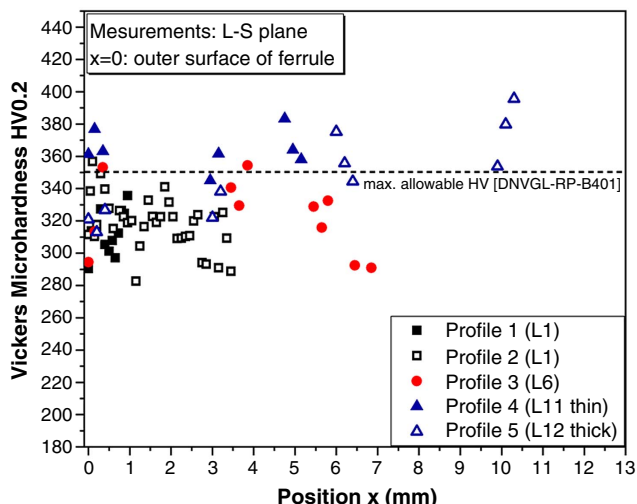


FIGURE 10. Microhardness ( $HV_{0.2}$ ) vs. position,  $x$ , in the cross-sectional direction on the L-S plane.  $X = 0$  mm represents the outside surface of the swaged section.

ASTM A923-14 standard (Figure 3[d]), the corrosion test described in Test Method C of the same standard was conducted to quantify the relative corrosion resistance and possibly confirm the presence of IMCs.<sup>30</sup> In all cases, no pitting was observed and the corrosion rate was below the 10 mdd acceptance criterion defined in the standard (Table 7). Consequently, the influence of possible IMC precipitation on HISC was not considered a causative factor.

### 3.8 | Other Observations

As shown in Figure 14(a), a suspected undercut, thought to be caused by machining, was observed all around the internal perimeter at the transition between the thinner portion of the swaged section and the thick portion. At that location, secondary microcracks were found away—approximately 5 cm radially—from the primary crack (Figure 14[b]). SEM analysis of the same castellation but at the main crack fracture surface confirmed the presence of a machining undercut of approximately 218  $\mu\text{m}$  and revealed a deeper secondary crack that extended approximately 992  $\mu\text{m}$  (Figure 14[c]).

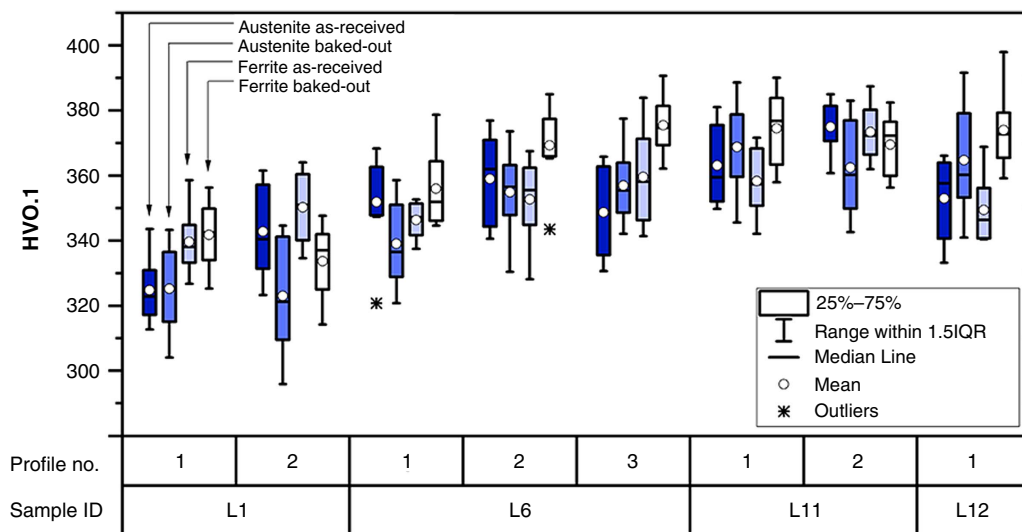
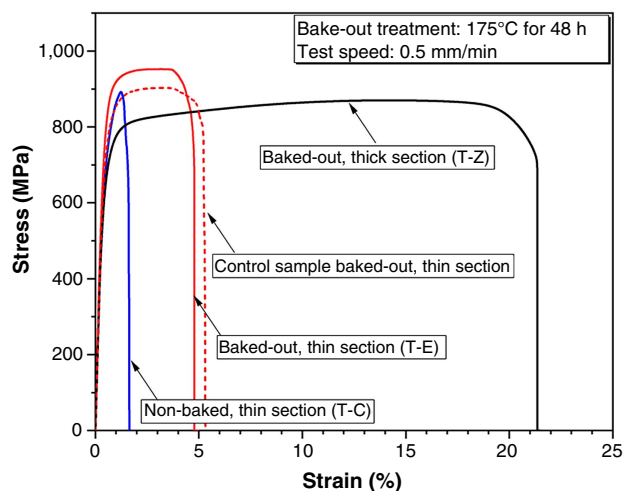


FIGURE 11. Microhardness ( $HV_{0.1}$ ) of austenite and ferrite individual grains along the swaged section before and after baking-out at 175°C for 48 h.

Table 6. Mechanical Properties of the Tensile Test Specimens

Sample ID	Swaged Section	Heat Treatment	0.2% YS (MPa)	UTS (MPa)	Elongation at Fracture (%)	Modulus of Toughness (MJ/m <sup>3</sup> )
Control	Thin	Baked-out <sup>(A)</sup>	775	902	5.31	44.04
T-A	Thin	Nonbaked	810	863	1.66	10.79
T-B	Thin	Nonbaked	724	897	1.47	9.46
T-C	Thin	Nonbaked	707	892	1.64	11.23
T-D	Thin	Nonbaked	711	839	1.15	6.43
T-E	Thin	Baked-out	832	952	4.78	41.94
T-F	Thin	Baked-out	770	944	4.11	32.28
T-Y	Thick	Baked-out	894	972	10.27	94.64
T-Z	Thick	Baked-out	599	870	21.35	178.38

<sup>(A)</sup> The control sample was baked-out prior to the machining and flattening.



**FIGURE 12.** Stress-strain curves of UNS S32760 for as received (*i.e.*, nonbaked) sample (T-C), samples from the thin section baked-out before (control sample) and after the flattening (T-E) and a baked-out sample from the thick portion of the swaged section (T-Z). The influence of residual hydrogen and swaging can be seen by the reduction of elongation to fracture and modulus of toughness for the four different conditions.

## DISCUSSION

### 4.1 | Influence of Microstructure and Manufacturing

The microstructure was found to be highly anisotropic in both the swaged and nonswaged portions of the component, typical of forged and cold-worked processes.<sup>41-42</sup> The austenite and ferrite regions were elongated in the working direction, leading to a fine—*i.e.*, between 22.6  $\mu\text{m}$  and 27.4  $\mu\text{m}$ —austenite spacing through-thickness, but a significantly larger spacing in the longitudinal direction. Indeed, some austenite and ferrite regions appeared to extend uninterrupted for several hundreds of microns, giving an austenite-free path of up to 185  $\mu\text{m}$ . Through-thickness cross-sectional LOM at three locations along the swaged section showed no apparent differences in the anisotropy index in the L-S plane (see Table 3). As cracking propagated primarily in the longitudinal direction of the component, the elongated grains led to an unfavorably oriented microstructure that might have facilitated crack propagation.<sup>21</sup> Although, suspected intragranular nitrides and intergranular precipitates were revealed by the electroetching methods (Table 1), the ASTM A923 test indicated no measurable reduction in localized corrosion performance at 50°C.

The additional cold-work introduced by swaging increased Vickers microhardness (HV0.2), on average, by 20% when compared to the stem of the component. The maximum average hardness measured in the transition part of the swaged portion exceeded the 350 HV allowable values suggested in DNVGL RP B401.<sup>36</sup> Although a direct quantitative comparison is not possible, at this location the results qualitatively exceeded the increase in hardness caused by cold-working measured by Francis, et al. In this regard, the authors found no noticeable influence of cold-working up to 35 HRC.<sup>10</sup>

Tensile test results illustrated the reversibility of the hydrogen embrittlement process and supported a HISC failure mode hypothesis, as shown by the increase in elongation to failure and toughness with baking. All nonbaked specimens showed little to no plasticity and a clear cleavage fracture mode close to the external surface exposed to hydrogen generated by CP. In this

regard, El-Yazgi and Hardie found that when the austenite content in a DSS increased to 35%, no recovery in ductility was observed at room temperature even after 3 y at ambient temperature post-thermal H charging.<sup>19</sup> In contrast, hydrogen removal by the bake-out heat treatment led to a recovery in mechanical properties and predominant ductile dimpled rupture. Furthermore, given that no significant differences were observed between the samples baked-out before and after the flattening step (Figure 12), it was concluded that the embrittlement seen in the nonbaked samples was primarily a result of their hydrogen content and not a consequence of the additional plastic deformation introduced during sample preparation.

### 4.2 | Fractography

Analysis of the fracture surface revealed that cracking was predominantly brittle cleavage, with mixed cleavage/rupture and dimple rupture areas at the thin end of the swaged section and near the castellations. In this regard, whereas the outer surface exhibited cleavage exclusively, there was a sharp transition to dimple rupture close to the internal surface of the swaged portion. Likewise, secondary cracking and significant plastic deformation were observed on the inner surface along the swaged section. Interestingly, a secondary crack was found at the first castellation, which might have been directly exposed to CP as suggested by the presence of calcium rich deposits on the adjacent fracture area.<sup>43</sup>

The EBSD maps presented in Figure 9 revealed that the crack propagated transgranularly and primarily through the ferrite regions. It arrested or changed the direction of propagation at austenite/ferrite boundaries (Figures 9[b] and [c]). The band contrast (BC) and the Kernel average misorientation (KAM) maps (Figures 9[a] and [d]), respectively, illustrate the unindexed defect traces nearby the crack, which correlate with the geometrically necessary dislocation (GND) boundaries revealed in the KAM map. GNDs are regarded as the fingerprint of deformation.<sup>44-45</sup> In TEM investigations these appear as the hotspots of strain localization in the material, typically known by cell or microband nomenclature.<sup>46</sup> Although, a comparison between the phase and KAM maps (Figures 9[b] and [d]) indicated that the GND boundaries, which arise due to deformation, were present in both phases, qualitatively, they seem to form predominantly within austenite. The concentration of GND boundaries in the austenite suggested that cracking nucleated rapidly in ferrite, while the austenite phase required extra work to be torn out to progress crack propagation. Thus, austenite could absorb more energy than ferrite before cracking. Nevertheless, in some regions cracking also crossed austenite grains.

The results presented herein agreed with Oltra and Bouillot who demonstrated—using secondary ion mass spectrometry of deuterium-charged DSS tensile coupons—that crack propagation occurs primarily through ferrite.<sup>47</sup> Later, Oltra, et al., determined that crack transitioned from ferrite to austenite accompanied by localized microcracking of austenite grains given sufficient deformation.<sup>48</sup> Indeed, the authors found hydrogen (deuterium) segregation only on austenite grains along the crack path, supporting the role of austenite as a “barrier” to crack propagation.<sup>47</sup>

Secondary cracks and limited branching were also found on T-L plane and cross-sectional (S-T) views. Secondary machining-cracks were further found by both LOM and SEM nucleating at the tip-end of a suspected machining defect located at the step-transition between the thin and the thick portions of the swaged section (Figure 14). A detailed analysis revealed that the suspected machining defect extended

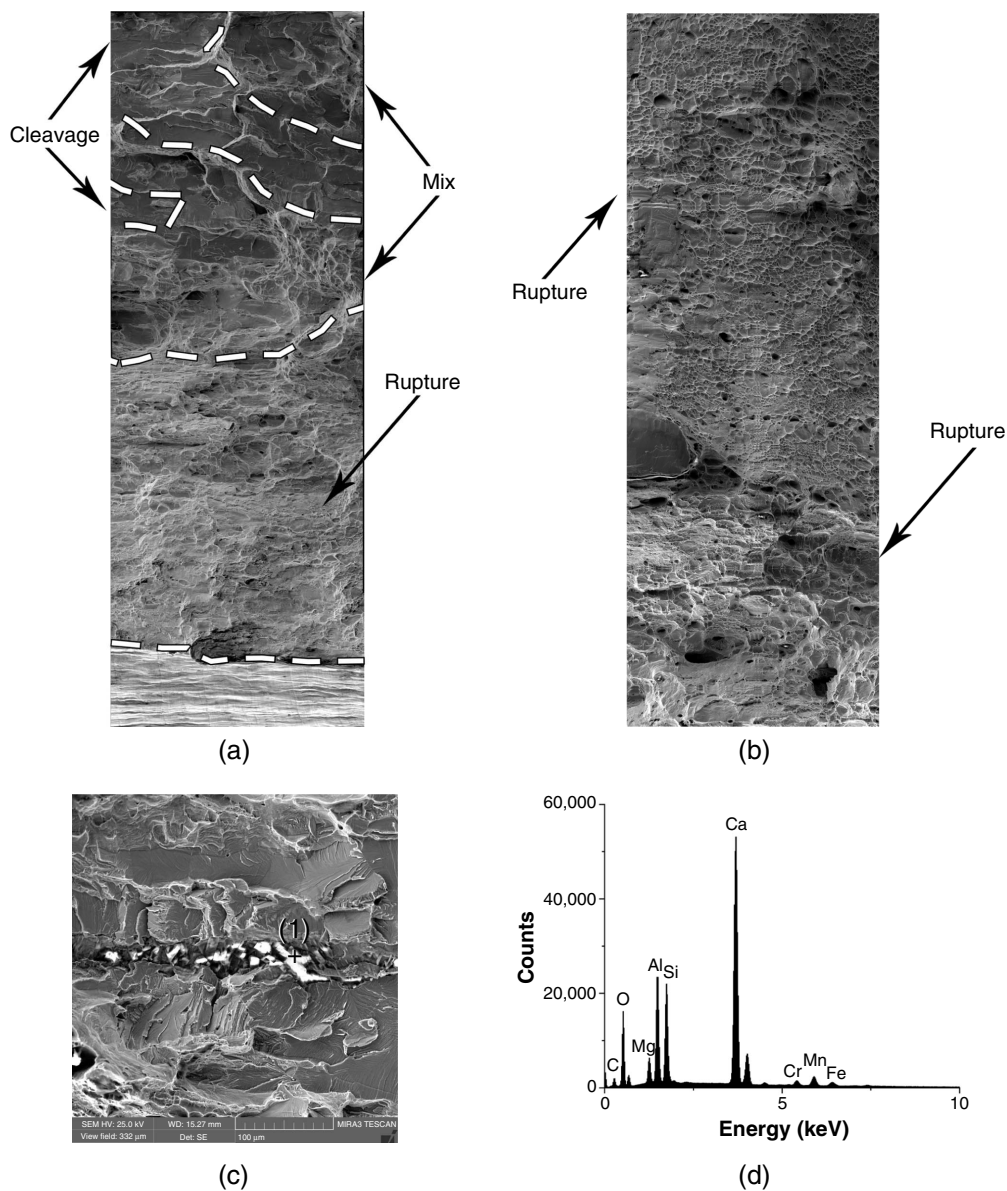


**FIGURE 13.** Fracture surface profile of tensile specimens from the outer to the inner surface (top and bottom of the images) (a) T-A and (b) T-Z. (c) shows the aligned inclusions surrounded by cleavage in areas of predominantly rupture fracture observed in sample T-E. (d) EDS analysis of the inclusions at 25 kV and a 15 mm of working distance. FE-SEM images were obtained with 15 kV, a working distance of 31 mm approximately and in resolution mode.

between 50 µm and 220 µm into the material, which might have locally increased the stress intensity factor. The secondary cracking along the main crack at the machining defect propagated up to approximately 950 µm to 1,000 µm from the sharp end of the undercut (Figure 14[c]).

Inclusions were observed on some of the tensile tests as seen in Figure 13(c). Inclusions were located in small cleavage

regions surrounded by predominantly rupture zones. These findings resemble the work of Zheng and Hardie who reported the presence of inclusions of various types (including manganese sulfide and calcium aluminate), associated with regions of "quasi-cleavage" on the fracture surfaces of precharged and thermally charged DSS.<sup>49</sup> The authors showed that inclusions played no direct role in crack initiation on samples tested in a

**Table 7. Corrosion Test Results**

Specimen	Total Area (dm <sup>2</sup> )	Initial Weight (g)	Final Weight (g)	Weight Loss (mg)	Corrosion Rate (mdd)
A	0.20586	26.2907	26.2894	1.3	6.3
B	0.2013	25.2691	25.2687	0.4	1.98

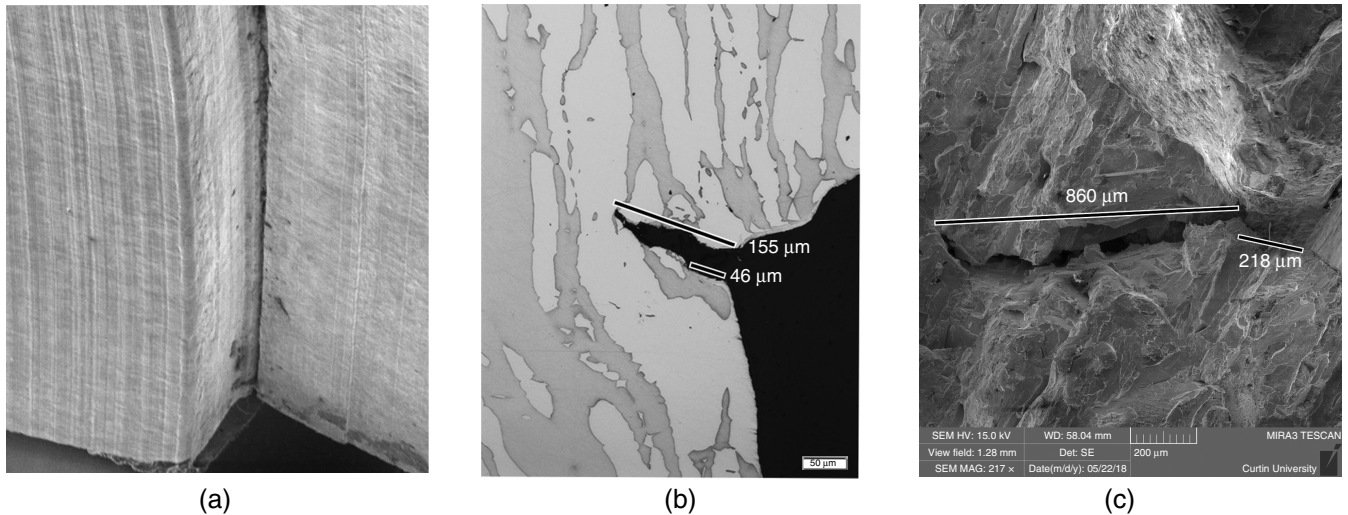


FIGURE 14. Machining defects: (a) macroscopic SE-SEM image, (b) secondary crack found 50 mm away from the main crack, and (c) main crack fracture surface at the defect location.

hydrogen atmosphere. Under those conditions, crack initiated at the surface on the ferrite phase as hydrogen was readily available. Cracking initiation, on the other hand, was associated with inclusions on precharged specimens that were subsequently tensile tested in an inert atmosphere. As in our work inclusions were found only during tensile testing of specimens that were precharged due to exposure to CP and not on the fracture surface of the failed components, it is possible that the inclusion/matrix boundary could have facilitated internal crack nucleation during tensile loading. Moreover, hydrogen release from inclusions during baking could explain the lower elongation to failure of samples extracted from the thin, swaged section when compared with the thick portion of the component (Figure 12).<sup>49</sup> In this regard, 175°C might have been insufficient to remove the entire diffusible hydrogen content.

4.3 | Failure Mechanism

The presence of more than 40 ppm of total dissolved hydrogen, which was in line with the amount of H measured after service exposure to CP and well above the values known to produce HISC of (S)DSS,<sup>20,35</sup> the predominantly cleavage fracture surface, the crack propagation across the ferrite regions, the presence of secondary cracking, and the reversibility observed in tensile tests support the HISC failure mechanism hypothesis.

An environmentally assisted failure such as HISC is always the result of a combination of factors, where the environment, the material and microstructure, and the overall stress state play decisive roles.<sup>50</sup> Because the failed component was exposed to seawater and given the direct electrical connection to the rest of the structure, hydrogen was introduced into the material by exposure to the CP system. At the thin end of the swaged section, atomic hydrogen generated by the CP system had multiple entry pathways, locally increasing the amount of diffusible hydrogen.

As hydrogen migrates primarily toward regions of high triaxial stress,<sup>51-54</sup> it is reasonable to hypothesize that cracking could have initiated at the first castellation, which may have acted as a local stress raiser. In this regard, Blanchard, et al., suggested that HISC can occur even with residual, trace-H amounts in the presence of high stress concentrations.<sup>23</sup>

Once the conditions for HISC are met, the authors postulated, a very small load would be required to extend a crack, either pre-existing or one that has already initiated.<sup>23</sup> Similarly, based on the results of service failure investigations, Cassagne and Busschaert emphasized the need to verify the absence of notches and sharp angles during design as well as undercuts after machining.<sup>6</sup> This hypothesis is supported in our work by the secondary cracks found at the bottom of the first castellation as well as the secondary cracking that started at the tip of the suspected machining defects. The initial crack may have propagated subsequently to the outer surface. Alternatively, cracking could have initiated at an external surface defect or internally at an inclusion or another volumetric flaw (as long as these are not too deep to not see hydrogen in service life), either at the austenite or ferrite phase as shown by Chou and Tsai.<sup>55</sup> Irrespective of the location of crack initiation, the crack tip(s) would have been directly exposed to hydrogen generated by CP once the crack reached the external surface. The hoop stress, then, would have opened the crack, facilitating its propagation in the longitudinal direction given the unfavorable grain orientation (Figure 15). The fact that cracking extended farther on the outer than the inner surface supports the notion that the primary crack propagation is likely to have started at the outer surface of the thinner portion of the swaged section.

It is proposed that the failure occurred in four stages:

- (i) hydrogen accumulation, (ii) crack initiation, (iii) crack

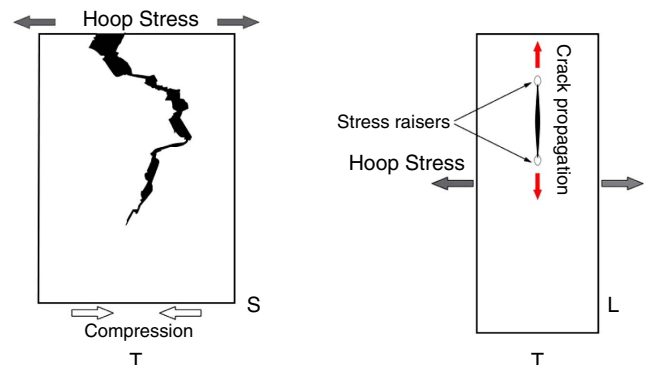


FIGURE 15. Proposed crack propagation mechanism.

propagation to the outer surface, and (iv) crack propagation in the longitudinal direction. The hydrogen accumulation period is associated with the time to reach the threshold hydrogen concentration,  $C_H$ , and it can be the rate-determining step.<sup>56</sup> Although, there can be multiple initiation points, a crack will reach a critical size in the area of highest total tensile stress first, assuming the availability of atomic hydrogen at this position. Once a crack reaches the critical flaw size, it can quickly propagate to the outer surface. Given that hydrogen would have been readily available at the outer surface, cracking could have finally propagated at a relatively fast rate in the longitudinal direction assisted by the hoop stress and unfavorable microstructure.

## CONCLUSIONS

In this work, the outcome of a comprehensive investigation on the failure of two subsea connectors made of UNS S32760 SDSS was presented. The study combined microstructural and fractographic characterization (with tools such as LOM and FE-SEM coupled with EDS and EBSD), corrosion testing, hydrogen content analysis, as well mechanical testing and microhardness mapping. The following conclusions were drawn.

> The predominately cleavage fracture surface, the presence of secondary cracks and mixed fracture surfaces, the total residual hydrogen content, the brittle fracture found in tensile tests in the nonbaked condition, and the recovery of properties after hydrogen bake-out strongly support HISC as the failure mechanism.

> The manufacturing process (forging and swaging) aligned the SDSS microstructure, reducing HISC resistance of the components. As a result, the longitudinal austenitic spacing, i.e., in the main crack propagation direction, exceeded DNVGL-RP-F112 coarse-fine threshold limit by a factor of up to six. This unfavorable microstructure could not have been detected by measuring the austenitic interspacing through-thickness, the suggested direction in the first edition of the Recommended Practice.

> The design and processing of the swaged section of the components could have increased the HISC susceptibility. Swaging led to an increase in hardness when compared to the solely forged and machined portion of the components, which was attributed to the added cold-work. Castellations and machining defects may have acted as stress raisers, likely facilitating and contributing to crack initiation.

## ACKNOWLEDGMENTS

We acknowledge the support of the John de Laeter Centre at Curtin University. We also thank colleagues and friends that were involved in this investigation, namely, Elaine Miller, Varun Ghodkay, Hoda Ehsani, William Rickard, Graeme Watson, Luke English, and Arne Bredin.

## References

- J. Charles, "Super Duplex Stainless Steels: Structure and Properties," Duplex Stainless Steels '91 (Beaune, Bourgogne, France: Proceedings. Les Éditions de Physique Les Ulis, 1991), p. 151-168.
- J.I. Skar, S. Olsen, *Corrosion* 73, 6 (2017): p. 655-665.
- API TR 938-C, "Use of Duplex Stainless Steels in the Oil Refining Industry" (Houston, TX: American Petroleum Institute, 2015).
- G. Krauss, "Stainless Steels," in *Steels: Processing, Structure, and Performance* (Metals Park, OH: ASTM International, 2005), p. 495-534.
- J.O. Nilsson, *Mater. Sci. Technol.* 8, 8 (1992): p. 685-700.
- T. Cassagne, F. Busschaert, "A Review On Hydrogen Embrittlement Of Duplex Stainless Steels," CORROSION 2005, paper no. 05098 (Houston, TX: NACE International, 2005).
- NACE/ASTM G193-12d, "Standard Terminology and Acronyms Relating to Corrosion" (West Conshohocken, PA: ASTM International, 2012).
- R. Johnsen, "Hydrogen Induced Stress Cracking of Duplex Stainless Steel in Seawater— What Do We Know and What is Still Unknown?," EUROCORR 2017, paper no. 72317 (Prague, Czech Republic: European Federation of Corrosion, 2017).
- A.A. El-Yazgi, D. Hardie, *Corros. Sci.* 38, 5 (1996): p. 735-744.
- R. Francis, G. Byrne, G.R. Warburton, *Corrosion* 53, 3 (1997): p. 234-240.
- T.S. Taylor, T. Pendlington, R. Bird, "Foinaven Super Duplex Materials Cracking Investigation," Offshore Technology Conference, paper no. OTC 10965 (Houston, TX: Offshore Technology Conference, 1999).
- S. Huizinga, B. McLaughlin, I.M. Hannah, S.J. Paterson, B.N.W. Snedden, "Failure of a Subsea Super Duplex Manifold Hub by HISC and Implications for Design," CORROSION 2006, paper no. 06145 (Houston, TX: NACE, 2006).
- G. Byrne, R. Francis, G. Warburton, M. Maligas, "The Selection of Superduplex Stainless Steel For Oilfield Applications," CORROSION 2004, paper no. 04123 (Houston, TX: NACE, 2004).
- NORSOK M-WA-01, "Design Guideline to Avoid Hydrogen Induced Stress Cracking in Subsea Duplex Stainless Steels" (Fornebu, Norway: Standards Norway, 2005).
- M. Solnørda, S. Wästberg, G. Heiberg, O. Hauås-Eide, *Meas. Control* 42, 5 (2009): p. 145-148.
- M. Aursand, G. Rørvik, L.A. Marken, I.M. Kulbotten, "Experiences with Hydrogen Induced Stress Cracking of Duplex Stainless Steel Components in Subsea Service with Cathodic Protection," CORROSION 2013, paper no. 2490 (Houston, TX: NACE, 2013).
- F. Iacoviello, M. Habashi, M. Cavallini, *Mat. Sci. Eng. A-Struct.* 224, 1-2 (1997): p. 116-124.
- A. Turnbull, R.B. Hutchings, *Mat. Sci. Eng. A* 177, 1 (1994): p. 161-171.
- A.A. El-Yazgi, D. Hardie, *Mater. Sci. Technol.* 16, 5 (2000): p. 506-510.
- G. Lauvstad, R. Johnsen, I. Asbjørnsen, M. Bjurström, C.G. Hjorth, *Corrosion* 66, 11 (2010): p. 115004-115013.
- W. Zheng, D. Hardie, *Corrosion* 47, 10 (1991): p. 792-799.
- DNVGL-RP-F112, "Duplex Stainless Steel - Design Against Hydrogen Induced Stress Cracking" (Høvik, Norway: DNV-GL, 2018).
- L. Blanchard, H. Dong, K. Sotoudeh, "Environmental Testing of Rolled and Hot Isostatically-Pressed Duplex Stainless Steels," CORROSION 2018, paper no. 11439 (Houston, TX: NACE, 2018).
- R.S. Treseder, R.P. Badrak, "Effect of Cold Working on SSC Resistance of Carbon and Low Alloy Steels - A Review," CORROSION 1997, paper no. 41 (Houston, TX: NACE, 1997).
- S.S. Chen, T.I. Wu, J.K. Wu, *J. Mater. Sci.* 39, 1 (2004): p. 67-71.
- J.-L. Crolet, M. Bonis, "Evaluation of the Resistance of Some Highly Alloyed Stainless Steels to Stress Corrosion Cracking in Hot Chloride Solutions Under High Pressures of CO<sub>2</sub> and H<sub>2</sub>S," CORROSION 1985, paper no. 232 (Houston, TX: NACE, 1985).
- ASTM E112-13, "Standard Test Methods for Determining Average Grain Size" (West Conshohocken, PA: ASTM International, 2013).
- ASTM E1181-02(2015), "Standard Test Methods for Characterizing Duplex Grain Sizes" (West Conshohocken, PA: ASTM International, 2015).
- MAT-2010080, "Technical Note— Metallographic Etching of Duplex Stainless Steels" (Oslo, Norway: Statoil ASA, 2010).
- ASTM A923-14, "Standard Test Methods for Detecting Detrimental Intermetallic Phase in Duplex Austenitic/Ferritic Stainless Steels" (West Conshohocken, PA: ASTM International, 2014).
- ASTM E384-17, "Standard Test Method for Microindentation Hardness of Materials" (West Conshohocken, PA: ASTM International, 2017).
- ASTM E92-17, "Standard Test Methods for Vickers Hardness and Knoop Hardness of Metallic Materials" (West Conshohocken, PA: ASTM International, 2017).
- ASTM E8/E8M-16a, "Standard Test Methods for Tension Testing of Metallic Materials" (West Conshohocken, PA: ASTM International, 2016).

34. ASTM E1019, "Standard Test Methods for Determination of Carbon, Sulfur, Nitrogen, and Oxygen in Steel, Iron, Nickel, and Cobalt Alloys by Various Combustion and Inert Gas Fusion Techniques" (West Conshohocken, PA: ASTM International, 2018).
35. R. Morana, L. Smith, K. Sotoudeh, S. Smith, "Validation of DNV RP F112 for Managing Hydrogen Induced Stress Cracking (HISC) in Super Duplex Stainless Steel for Subsea Applications," CORROSION 2018, paper no. 10974 (Houston, TX: NACE, 2018).
36. DNVGL-RP-B401, "Cathodic Protection Design" (Høvik, Norway: DNV-GL, 2017).
37. U.H. Kivisäkk, *Mat. Sci. Eng. A-Struct.* 527, 29-30 (2010): p. 7684-7688.
38. ASTM A1049/A1049M-18, "Standard Specification for Stainless Steel Forgings, Ferritic/Austenitic (Duplex), for Pressure Vessels and Related Components" (West Conshohocken, PA: ASTM International, 2018).
39. A790/A790M-18, "Standard Specification for Seamless and Welded Ferritic/Austenitic Stainless Steel Pipe" (West Conshohocken, PA: ASTM International, 2018).
40. R. Francis, G. Warburton, "Use of Zeron 100 for Fasteners," RA®Materials Report, TN769, 2008.
41. R. Gunn, "Chapter 3: Microstructure," in *Duplex Stainless Steels: Microstructure, Properties and Applications* (Cambridge, UK: Woodhead Publishing, 1997), p. 24-49.
42. J. Keichel, J. Foct, G. Gottstein, *ISIJ Int.* 43, 11 (2003): p. 1781-1787.
43. W.H. Hartt, C.H. Culberson, S.W. Smith, *Corrosion* 40, 11 (1984): p. 609-618.
44. Y.I. Golovin, *Phys. Solid State* 50, 12 (2008): p. 2205-2236.
45. T. Hajilou, Y. Deng, B.R. Rogne, N. Kheradmand, A. Barnoush, *Scr. Mater.* 132 (2017): p. 17-21.
46. D.A. Hughes, N. Hansen, D.J. Bammann, *Scr. Mater.* 48 (2003): p. 147-153.
47. R. Oltra, C. Bouillot, "Experimental Investigation of the Role of Hydrogen in Stress Corrosion Cracking of Duplex Stainless Steels," Hydrogen Transport and Cracking—Proceedings of a Conference Held at The National Physical Laboratory (Teddington, UK: The Institute of Materials, 1994), p. 17-26.
48. R. Oltra, C. Bouillot, T. Magnin, *Scr. Mater.* 35, 9 (1996): p. 1101-1105.
49. W. Zheng, D. Hardie, *Corros. Sci.* 32, 1 (1991): p. 23-36.
50. R.P. Gangloff, "6.02," in *Comprehensive Structural Integrity*, eds. I. Milne, R.O. Ritchie, B. Karihaloo, vol. 6 (New York, NY: Elsevier Science, 2003), p. 31-101.
51. R.D. Kane, M.S. Cayard, "Roles of H<sub>2</sub>S in the Behavior of Engineering Alloys: A Review of Literature and Experience," CORROSION 1998, paper no. 98274 (Houston, TX: NACE, 1998).
52. W.W. Gerberich, T. Livne, X.F. Chen, M. Kaczorowski, *Metall. Trans. A-Phys. Metall. Mater. Sci.* 19, 5 (1988): p. 1319-1334.
53. A.R. Troiano, *Metallogr. Microstruct. Anal.* 5, 6 (2016): p. 557-569.
54. A.R. Troiano, *Corrosion* 15, 4 (1959): p. 57-62.
55. S.L. Chou, W.T. Tsai, *Mater. Chem. Phys.* 60, 2 (1999): p. 137-142.
56. S. Lynch, *Corros. Rev.* 30, 3-4 (2012): p. 105-123.